# Optimization of propagation-based x-ray phase-contrast tomography for breast cancer imaging

**P Baran**[1], **S Pacile**[2,3], **Y I Nesterets**[4,5], **S C Mayo**[4], **C Dullin**[6],
**D Dreossi**[2], **F Arfelli**[2,7], **D Thompson**[4,5], **D Lockie**[8],
**M McCormack**[9], **S T Taba**[10], **F Brun**[2,3], **M Pinamonti**[11],
**C Nickson**[12], **C Hall**[13], **M Dimmock**[14], **F Zanconati**[11],
**M Cholewa**[15], **H Quiney**[1], **P C Brennan**[10], **G Tromba**[2]
**and T E Gureyev**[1,4,5,16,17]

[1] ARC Centre of Excellence in Advanced Molecular Imaging, School of Physics, The University of Melbourne, Parkville 3010, Australia
[2] Elettra—Sincrotrone, 34149 Basovizza, Trieste, Italy
[3] Department of Engineering and Architecture, University of Trieste, 34127 Trieste, Italy
[4] Commonwealth Scientific and Industrial Research Organisation, Clayton 3168, Australia
[5] School of Science and Technology, University of New England, Armidale 2351, Australia
[6] Department of Diagnostic and Interventional Radiology, University Hospital Goettingen, 37075 Goettingen, Germany
[7] Department of Physics, University of Trieste and INFN, 34127 Trieste, Italy
[8] Maroondah BreastScreen, Ringwood East 3135, Australia
[9] TissuPath Specialist Pathology Services, Mount Waverley 3149, Australia
[10] Faculty of Health Sciences, University of Sydney, Lidcombe 2141, Australia
[11] Department of Pathology, Academic Hospital of Trieste, 34128 Trieste, Italy
[12] Melbourne School of Population and Global Health, The University of Melbourne, Carlton 3053, Australia
[13] Australian Synchrotron, Clayton 3168, Australia
[14] Department of Medical Imaging and Radiation Sciences, Monash University, Clayton 3800, Australia
[15] Department of Biophysics, Faculty of Mathematics and Natural Sciences, University of Rzeszow, 35-310 Rzeszow, Poland
[16] School of Physics and Astronomy, Monash University, Clayton 3800, Australia

E-mail: Timur.Gureyev@unimelb.edu.au

[17] Author to whom any correspondence should be addressed.

**Abstract**

The aim of this study was to optimise the experimental protocol and data analysis for *in-vivo* breast cancer x-ray imaging. Results are presented of the experiment at the SYRMEP beamline of Elettra Synchrotron using the propagation-based phase-contrast mammographic tomography method, which incorporates not only absorption, but also x-ray phase information. In this study the images of breast tissue samples, of a size corresponding to a full human breast, with radiologically acceptable x-ray doses were obtained, and the degree of improvement of the image quality (from the diagnostic point of view) achievable using propagation-based phase-contrast image acquisition protocols with proper incorporation of x-ray phase retrieval into the reconstruction pipeline was investigated. Parameters such as the x-ray energy, sample-to-detector distance and data processing methods were tested, evaluated and optimized with respect to the estimated diagnostic value using a mastectomy sample with a malignant lesion. The results of quantitative evaluation of images were obtained by means of radiological assessment carried out by 13 experienced specialists. A comparative analysis was performed between the x-ray and the histological images of the specimen. The results of the analysis indicate that, within the investigated range of parameters, both the objective image quality characteristics and the subjective radiological scores of propagation-based phase-contrast images of breast tissues monotonically increase with the strength of phase contrast which in turn is directly proportional to the product of the radiation wavelength and the sample-to-detector distance. The outcomes of this study serve to define the practical imaging conditions and the CT reconstruction procedures appropriate for low-dose phase-contrast mammographic imaging of live patients at specially designed synchrotron beamlines.

Keywords: x-ray imaging, mammography, breast cancer, computed tomography, x-ray phase contrast

(Some figures may appear in colour only in the online journal)

## Introduction

Breast cancer is one of the two leading causes of cancer death among women in most developed countries, next to lung and bronchus cancer (Siegel *et al* 2016). This is also the most frequent cancer among women, with an estimated 1.67 million new cases diagnosed in 2012, with the numbers consistently increasing around the world (Ferlay *et al* 2015). The most significant impact on the success of the treatment is achieved by precise and early diagnosis. The rate of mortality is stable in more developed countries and is increasing in less developed regions (Ferlay *et al* 2015). Mortality stability has been largely achieved through mammographic screening, as well as improved cancer treatment. Two-view x-ray mammography imaging is currently the main diagnostic technique used for screening women over 40 years of age.

The key limitation of mammography is the overlapping of breast tissue layers in the two-dimensional (2D) projection images, which can produce false positive (normal structures appear suspicious) and false negative (camouflaged cancer) results (Ciatto *et al* 2013). The

sensitivity of 2D mammography is approximately 70% (Alakhras *et al* 2013), which means that for 30% of women diagnosed with breast cancer abnormalities were not found in mammograms between 12 and 24 months before their diagnosis (Elmore *et al* 2005). The mammographic accuracy has been improved by the recent introduction of digital breast tomosynthesis (DBT) and breast-dedicated computed tomography (CT) which eliminate the problem of overlying tissues in conventional 2D images (Michell *et al* 2012, Gazi *et al* 2016). However, the small difference in x-ray attenuation, in particular between the glandular and tumour tissues, still constitutes a problem for these methods (Mittone *et al* 2014).

In recent years, the development of phase-contrast x-ray imaging techniques, which make use of refraction of x-rays in the body, have shown promising results for improving the breast cancer diagnosis (Pagot *et al* 2005, Sztrokay *et al* 2012, Diemoz *et al* 2012, Keyriläinen *et al* 2011). Phase-contrast imaging methods, such as grating-based CT, analyser-based CT or propagation-based CT (PB-CT), provide 3D images with better contrast-to-noise ratio compared to standard x-ray imaging techniques (Zhao *et al* 2012, Nesterets and Gureyev 2014). Importantly, these results can be achieved with smaller radiation doses delivered to the breast (Gureyev *et al* 2013). The PB-CT method, in particular, does not require any x-ray optical elements (such as the analyser crystals used in analyser-based CT) and is easier to implement in practice compared to other x-ray phase-contrast approaches (Keyrilainen *et al* 2010, Bravin *et al* 2013, Coan *et al* 2013, Olivo *et al* 2013, Gureyev *et al* 2014a). The effective use of x-ray phase information in PB-CT is made possible through specialized image processing algorithms based on the Homogeneous Transport of Intensity equation (TIE-Hom) (Paganin *et al* 2002). The use of this method allows one to effectively reduce image noise, while preserving the edge sharpness in the image (Pacile *et al* 2015, Nesterets *et al* 2015, Longo *et al* 2016).

An optimization of the main parameters of the PB-CT technique is necessary for translation of this method into clinical practice. In this paper, we present the results that build upon our previous studies at the synchrotron radiation for medical physics (SYRMEP) beamline of elettra synchrotron (Pacile *et al* 2015) and at the imaging and medical beamline (IMBL) of the Australian Synchrotron (Nesterets *et al* 2015), which were aimed at the development of the PB-CT mammography technique. In the present study we compared the results obtained with different experimental setups, such as different propagation distances and energies, and subsequently evaluated the image acquisition protocols as well as the image reconstruction algorithms. The collected x-ray projection images were optionally phase retrieved using the TIE-Hom method (Paganin *et al* 2002). Subsequently, 3D images of the breast tissue were reconstructed using different CT methods, such as simultaneous iterative reconstruction technique (SIRT) (Van der Sluis and van der Vorst 1990), iterative filtered back projection (iFBP) (Myers *et al* 2010) and several others. A quantitative evaluation of the reconstructed images was performed using several objective image quality metrics, such as the spatial resolution, signal-to-noise ratio (SNR) and the intrinsic quality characteristic $Q_s$ (Gureyev *et al* 2014b). We carried out a radiological assessment of the obtained PB-CT images by a relatively large group of 13 medical imaging specialists, and demonstrated for the first time that the subjective scores assigned by these specialists to different images were generally in good agreement with the objective image quality indices of the same PB-CT images of the breast tissue specimen. The image quality indices obtained for an extended range of examined parameters (e.g. different distances and energies) were consistent with the previously published theoretical results of propagation-based phase contrast analysis. Also, for the first time in this work we have performed a successful cross-identification of features and comparison between histological images and x-ray images obtained with PB-CT of breast tissues.

**Table 1.** Geometrical magnification ($M = 1 + R_2/R_1$, $R_1$ is the source-to-sample distance, $R_2$ is the sample-to-detector distance), effective free-space propagation distance ($R' = R_2/M$) and values of effective pixel size of the Hamamatsu (100 $\mu$m physical size, $h'_H$ effective size) and Dalsa (54 $\mu$m physical size in $2 \times 2$ binning mode, $h'_D$ effective size) detectors.

| $M$ | $R_2$ (m) | $R'$ (m) | $h'_H$ ($\mu$m) | $h'_D$ ($\mu$m) |
|---|---|---|---|---|
| 1.405 | 9.31 | 6.63 | 71.2 | 38.4 |
| 1.080 | 1.85 | 1.71 | 92.6 | 50.0 |
| 1.007 | 0.16 | 0.16 | 99.3 | 53.6 |

## Materials and methods

### Experimental setup

The CT scans were performed at the SYRMEP beamline of the Elettra synchrotron in Trieste, Italy. This beamline utilises a bending magnet to provide a monochromatic, nearly parallel, laminar x-ray beam with an area of about $160 \times 3\,\text{mm}^2$ at the distance of $R_1 = 23$ m from the source. A Si (1 1 1) double-crystal monochromator is used in the Bragg configuration to deliver an x-ray beam in the energy range between 8.5 keV and 38 keV with an energy resolution of $\Delta E/E = 10^{-3}$ (Tromba *et al* 2011, Longo *et al* 2016). In this study two different detectors were used: Hamamatsu CMOS Flat Panel Sensor C9252DK-14 and DALSA Argus high-resolution CCD TDI sensor. The Hamamatsu detector was used in the partial scan mode, which had a smaller pixel size $100 \times 100\,\mu\text{m}^2$ at the expense of the reduced field of view, compared to the full scan mode of the same detector. This detector has a CsI scintillator directly deposited on a 2D photodiode array. The Dalsa detector was used in the $2 \times 2$ binning mode with an effective pixel size $54 \times 54\,\mu\text{m}^2$. Geometrical image magnification was taken into account in the evaluation of the effective pixel size of the detectors and sample-to-detector distances (table 1). The samples were imaged at three different energies: 32, 35 and 38 keV, in PB-CT mode using four different levels of photon statistics (see table 3 for the associated radiation doses). The CT scans were collected at three different sample-to-detector distances $R_2 = 0.16$, 1.85 and 9.31 m, the latter resulted in strongest phase-contrast. Each scan contained 2000 projections collected with 0.18° angular step over 360°. For correction of the x-ray projections, 40 dark current images and 40 flat field images were also collected, half before and half after each sample scan.

### Breast tissue sample

One human breast tissue specimen (figure 1), excised during a surgical left mastectomy procedure, was prepared for x-ray phase-contrast CT imaging and for histological examination. The sample with a malignant lesion was provided by the Department of Pathological Anatomy, University of Trieste Medical School, Cattinara Hospital, Trieste, Italy. The sample was taken from a 67 year-old woman with fibro-adipose breast parenchyma. During the histological examination multiple foci of intraductal papillomatosis and sclerosing adenosis were found. Moreover, histological examination found invasive ductal carcinoma, moderately differentiated (grade 2) with solid-trabecular and focally lobular-like aspects. The maximum diameter of the tumour was 27 mm. For imaging, the sample was fixed in formalin and sealed hermetically in a polyethylene container. The specimen was approximately 12 cm by 7.5 cm transversely and about 4 cm thick. Note that the transverse dimensions of the sample were
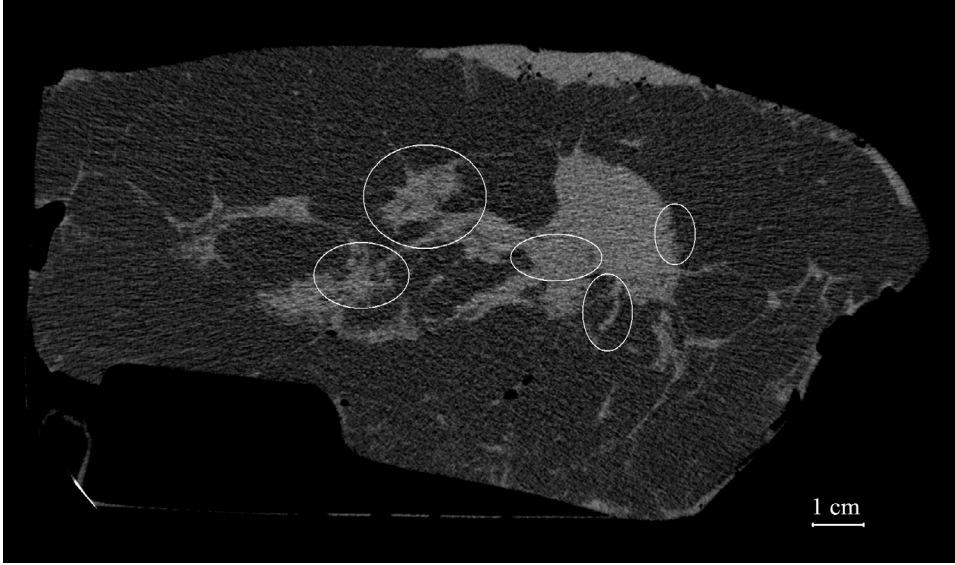
**Figure 1.** Reference image of breast tissue sample used in the radiological assessment (SIRT reconstruction from 1000 projections with 1000 iterations, $R_2 = 0.16$ m, $E = 32$ keV, Dose $= 2$ mGy). This image represents an approximation for the conventional (absorption-based or 'contact') mammographic image, with the best overall image quality achieved by the use of different reconstruction methods from the data collected at the shortest propagation distance at a given radiation dose. White ovals represent five regions-of- interest (ROIs) which were used for rating in the radiological assessment.

consistent with the conditions of full breast CT imaging, while the thickness of the sample was also larger than the height of the x-ray beam.

*Radiation dose estimation*

During the experiment, an ion chamber (IC) was installed in the x-ray beam. The readings from the IC, which were used for measuring the photon fluence rate, were recorded during the CT data acquisition. In order to calculate the mean absorbed dose ($D_{abs}$) of the breast tissue, a numerical phantom with the cross-section schematically depicted in figure 2 (Dance 1990, Protection and Measurements 2004) was used.

The phantom simulates the breast tissue with radius $r$ (in cm) and composed of 50w% gland tissue and 50w% adipose tissue (Hammerstein *et al* 1979), surrounded by adipose tissue (simulating the skin layer) enclosed inside a cylinder of radius $R_{out}$ (in cm). Using this phantom, the mean absorbed dose can be calculated by converting the photon fluences in the sample plane as follows (Johns and Yaffe 1985, Nesterets and Gureyev 2014, Nesterets *et al* 2015):

$$D_{abs}(\text{mGy}) = \frac{2}{\pi} 1.602 \times 10^{-10} \frac{R_{out}(\text{cm})}{r^2 (\text{cm}^2)} \frac{R_{abs,r} \, \Phi \, (\text{ph cm}^{-2}) \, E(\text{keV})}{\rho_r (\text{g cm}^{-3})} \tag{1}$$

Here $R_{abs,r}$ is the fraction of x-ray energy incident on the phantom which is absorbed in the glandular tissue, $\Phi$ is the incident photon fluence (in photons per cm$^2$), $\rho_r$ is the mass density
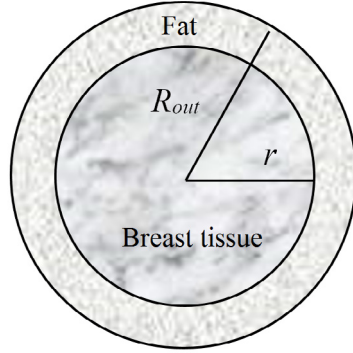
**Figure 2.** A schematic diagram of the numerical phantom used for mean glandular dose calculations (Nesterets *et al* 2015).

**Table 2.** Values of the $R_{abs,r}$ calculated using MC simulations for the phantom shown in figure 2 for three energies used in the experiment.

| | Photon energy $E$ (keV) | | |
|---|---|---|---|
| | 32 | 35 | 38 |
| $R_{abs,r}$ | 0.455 56 | 0.404 28 | 0.358 41 |

of the glandular tissue (in g cm$^{-3}$) and $E$ is the x-ray energy (in keV). The $R_{abs,r}$, values were calculated using Monte Carlo (MC) simulations with 5 cm and 4.5 cm for $R_{out}$ and $r$, respectively (Nesterets *et al* 2015), assuming that the entire phantom (unlimited along its axis) is uniformly illuminated by the x-ray beam. These values correspond to the dimensions of the sample used in the experiment. Results of this simulation for three different energies are shown in table 2. As mentioned above, for each energy, scans were made with four different levels of photon statistics, achieved by utilising Aluminium filters of varying thickness in combination with variable exposure time (table 3).

*CT reconstruction procedure*

X-TRACT (Gureyev *et al* 2011) and STP (Brun *et al* 2015) software were used for CT data processing and analysis which included data pre-processing and CT reconstruction. The pre-processing of projection images contained the following steps:

(1) dark current correction, consisting of subtraction of mean dark current image (collected with no x-ray illumination) from the datasets and from the flat-field images in order to remove the detector dark current contribution,
(2) flat-field correction, using images collected with the x-ray illumination, but without the sample, to correct for uneven illumination,
(3) optional phase retrieval, using the TIE-Hom algorithm (Paganin *et al* 2002),
(4) ring removal filter, for reducing ring artifacts caused by imperfect detector pixel elements (Boin and Haibel 2006, Brun *et al* 2013).

The TIE-Hom algorithm was optionally applied to the projection data sets, in order to optimally exploit the phase information, with different values of $\delta/\beta$ ratio. Here the $\beta$ value, which constitutes the imaginary part of the complex refractive index $n = 1 - \delta + i\beta$, is related to the

**Table 3.** Values of the mean glandular absorbed doses for breast tissue sample calculated by using the cylindrical numerical phantom shown in figure 2 (with the outer radius $R_{out} = 5$ cm and the inner radius $r = 4.5$ cm). Only the data corresponding to scans with the Hamamatsu detector is given here, as the scans collected with the Dalsa detector have not been used in the radiological assessment in the present study.

| | | Mean glandular absorbed doses (mGy) | | |
| | | $R_2$ (m) | | |
| $E$ (keV) | Photon statistics | 0.16 | 1.85 | 9.31 |
|---|---|---|---|---|
| 32 | High | 114.51 | 150.13 | 277.36 |
| | Medium | 14.63 | 19.08 | 34.67 |
| | Low | 7.32 | 9.22 | 17.18 |
| | Very low | 4.13 | 4.74 | 8.43 |
| 35 | High | 86.87 | 101.39 | 183.6 |
| | Medium | 10.79 | 13.15 | 26.1 |
| | Low | 5.58 | 6.51 | 11.44 |
| | Very low | 2.81 | 3.43 | 8.22 |
| 38 | High | 82.98 | 100.4 | 189.88 |
| | Medium | 10.41 | 12.55 | 23.77 |
| | Low | 4.87 | 7.57 | 9.89 |
| | Very low | 2.29 | 3.77 | 5.32 |

absorption, while the $\delta$ value, is related to the phase shift (Paganin *et al* 2002). The application of the TIE-Hom algorithm is particularly useful for imaging objects consisting of components with similar x-ray attenuation properties. For each energy, two different $\delta/\beta$ values were used. The first value was close to the theoretical value (TS-Imaging website 2016) of the relative $\delta/\beta$-value for glandular tissue in adipose tissue ($\delta/\beta = 870, 978, 1083$ for 32, 35 and 38 keV, respectively), while the second one was equal to one half of the first value. The latter value of $\delta/\beta$ was included into the study in order to test the hypothesis that such 'partially phase retrieved' image can be approximated by a mixture of the raw phase-contrast image, which typically has sharp edges, and the phase-retrieved image, which typically has better grey-scale differentiation for soft tissues, can potentially deliver an optimal combination of the two desirable properties (edge sharpness and soft tissue differentiation).

Normalised projections were converted to sinograms after pre-processing, and each sinogram was used to reconstruct the (dimensionless) distribution of the imaginary part of the complex refractive index, $\beta(x, y, z_0) = (\lambda/4\pi)\mu(x, y, z_0)$, within a single transverse slice of the sample ($\lambda$ is the x-ray wavelength and $\mu$ is the linear attenuation coefficient). In this study several different CT reconstruction algorithms were used, but due to the article space constraints, the results obtained with only two algorithms are included in the present paper: iterative filtered back-projection (iFBP), which is available in X-TRACT software, and simultaneous iterative reconstruction technique (SIRT), which is available in STP software. A detailed analysis of the results obtained with other CT reconstruction algorithms will be presented in a separate publication.

*Radiological assessment*

The radiological assessment was conducted on the basis of PB-CT x-ray images with acceptable radiation doses obtained during the experiment. Thirteen imaging specialists (seven radiologists and six diagnostic radiographers), each with over five years' experience in assessing

radiologic images, participated in the assessment. In the current stage of the evaluation, 81 images obtained with the Hamamatsu detector and different experimental parameters (distances and energies) were assessed. All images were reconstructed using two algorithms, iFBP and SIRT (the latter using 400 and 1000 iterations), following the application of the TIE-Hom phase retrieval algorithm with two different values of $\delta/\beta$ ratio (depending on the energy) and also without phase-retrieval algorithm. For each of the reconstructions, only one half of the collected projections (i.e. 1000) were used in order to reduce the effective dose to an acceptable level (around 4 mGy). The imaging specialists were asked to assess 6 image attributes within the 5 regions of interest (ROIs) outlined in the image (figure 1), in comparison with the same ROIs in the selected reference image (obtained at $R_2 = 0.16$ m and $E = 32$ keV, without phase retrieval), which corresponds to standard CT. The reference image was obtained using the SIRT algorithm (with 1000 iterations), because it gave us the best results for the images without phase contrast. The following attributes of the images were rated: soft tissue contrast (degree of differentiation of the densities of various soft tissue regions), edge sharpness (clarity of definition of edges and outlines of structures), soft tissue interfaces (clarity of visualization of interfaces between different soft tissue elements), spiculations (sharpness of reproduction of spiculations), artefacts (distractiveness of image mottle and other artefacts) and image noise (distractiveness of noise in the image). Each attribute was rated using a five-point scoring scale. The meaning of the rating scores was as follows: the fulfilment of the corresponding criteria in the new image was clearly better than $(+2)$; slightly better than $(+1)$; equal to $(0)$; slightly worse than $(-1)$; and clearly worse than $(-2)$ the fulfilment of that criteria in the reference image. For each image the mean values of all attributes were calculated. All images were assessed using primary reporting workstations with 5 megapixel monitors, which were calibrated to the grayscale standard display function (National Electrical Manufacturers Association 2011). Ambient lighting did not exceed 40 lux.

## Results

### Quantitative image assessment

The results of the radiological image assessment have confirmed that the propagation (sample-to-detector) distance was the most important variable of the experiment. The highest values in radiological scoring were consistently achieved for images obtained at the longest propagation distance. Additionally, images obtained at 32 keV received better scores on average compared to the other energies. Images, for which the TIE-Hom algorithm was applied, received higher scores than images reconstructed without phase retrieval. In order to objectively assess the images used in the radiological assessment, the values of three 'no-reference' indices, including the signal-to-noise ratio (SNR), the spatial resolution ($\Delta r$) and the intrinsic quality characteristic ($Q_s$) (Gureyev *et al* 2014a, Gureyev *et al* 2014b) were calculated, using X-TRACT software. For each image, two values for each of the above indices were obtained, using the same size area ($128 \times 128$ pixels), one inside and one outside the lesion. Within these areas, we calculated, using X-TRACT software, the mean of the pixel intensity values and its standard deviation. The SNR was then evaluated as the ratio of the mean to the standard deviation. The spatial resolution was calculated from the power spectrum of image noise (which was defined as the difference between the value of intensity in a given pixel and the mean intensity value within the area). Assuming that the incident photon flux within the selected small uniformly illuminated area was spatially stationary, ergodic and had Poisson statistics, it was possible to find the width of the system PSF by measuring the effective width of the power spectrum of the image noise. Indeed, while the power spectrum of incident

**Table 4.** The values of no-reference objective indices for images reconstructed with iFBP and SIRT (1000 iterations) algorithms, calculated inside the lesion with full phase retrieval (phr), half phase retrieval (0.5 phr) and no phase retrieval (none).

| Rank of $R'\lambda$ | $R_2$ (m) | $E$ (keV) | Phase retrieval | iFBP | | | SIRT 1000 | | |
|---|---|---|---|---|---|---|---|---|---|
| | | | | Spatial resolution ($\mu$m) | SNR | $Q'_s \cdot 10^{-2}$ ($\mu$m$^{-1}$) | Spatial resolution ($\mu$m) | SNR | $Q'_s \cdot 10^{-2}$ ($\mu$m$^{-1}$) |
| 1 | 0.16 | 38 | phr | 227 | 5.53 | 2.43 | 245 | 7.09 | 2.89 |
| | | | 0.5 phr | 218 | 6.53 | 3.00 | 227 | 7.15 | 3.14 |
| | | | None | 218 | 5.11 | 2.34 | 221 | 6.89 | 3.11 |
| 2 | 0.16 | 35 | phr | 224 | 5.72 | 2.55 | 245 | 7.98 | 3.26 |
| | | | 0.5phr | 221 | 6.53 | 2.96 | 241 | 7.67 | 3.19 |
| | | | None | 217 | 5.10 | 2.35 | 235 | 7.16 | 3.04 |
| 3 | 0.16 | 32 | phr | 225 | 5.56 | 2.47 | 228 | 7.34 | 3.21 |
| | | | 0.5 phr | 221 | 6.19 | 2.79 | 224 | 7.32 | 3.27 |
| | | | none | 217 | 5.14 | 2.37 | 220 | 6.29 | 2.87 |
| 4 | 1.85 | 38 | phr | 233 | 11.81 | 5.06 | 259 | 13.12 | 5.07 |
| | | | 0.5 phr | 223 | 12.08 | 5.41 | 245 | 11.48 | 4.68 |
| | | | None | 192 | 6.80 | 3.55 | 211 | 8.43 | 3.99 |
| 5 | 1.85 | 35 | phr | 227 | 9.46 | 4.17 | 252 | 11.33 | 4.50 |
| | | | 0.5 phr | 220 | 8.47 | 3.85 | 238 | 11.02 | 4.62 |
| | | | None | 188 | 5.39 | 2.87 | 208 | 6.96 | 3.35 |
| 6 | 1.85 | 32 | phr | 233 | 9.30 | 3.99 | 248 | 11.78 | 4.74 |
| | | | 0.5 phr | 225 | 4.95 | 2.20 | 237 | 10.64 | 4.50 |
| | | | None | 192 | 6.25 | 3.26 | 208 | 7.86 | 3.78 |
| 7 | 9.31 | 38 | phr | 146 | 10.94 | 7.49 | 218 | 14.00 | 6.42 |
| | | | 0.5 phr | 142 | 7.98 | 5.62 | 217 | 10.65 | 4.91 |
| | | | None | 105 | 1.78 | 1.70 | 173 | 4.22 | 2.44 |
| 8 | 9.31 | 35 | phr | 139 | 13.51 | 9.74 | 249 | 14.81 | 5.94 |
| | | | 0.5 phr | 140 | 9.75 | 6.98 | 223 | 12.30 | 5.52 |
| | | | None | 99 | 2.74 | 2.76 | 171 | 5.12 | 2.99 |
| 9 | 9.31 | 32 | phr | 144 | 13.58 | 9.41 | 232 | 15.77 | 6.81 |
| | | | 0.5 phr | 140 | 10.69 | 7.65 | 220 | 12.48 | 5.68 |
| | | | None | 108 | 2.86 | 2.65 | 171 | 5.05 | 2.96 |
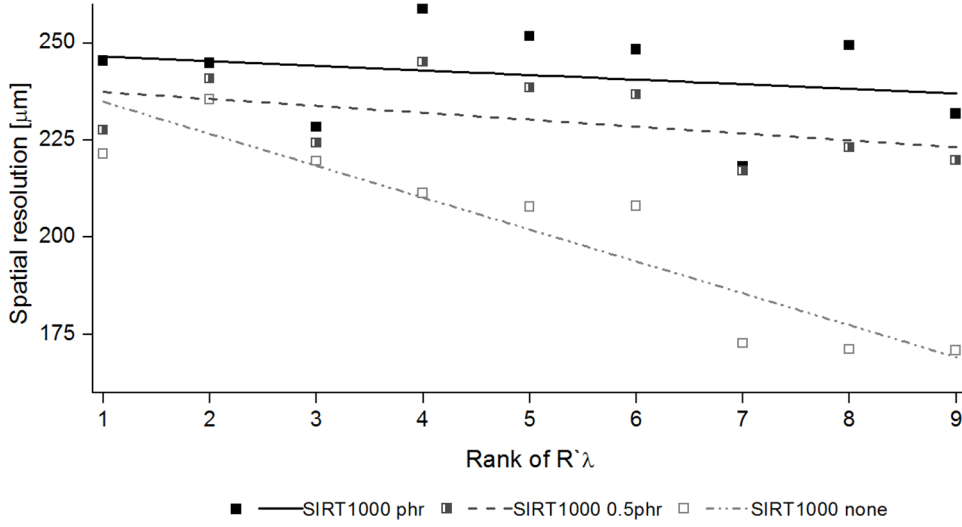
**Figure 3.** The values of spatial resolution measured inside the lesion for images reconstructed with SIRT (1000 iterations) algorithm with none, half (0.5 phr) and full (phr) phase retrieval.

white noise was uniform, the convolution with the detector PSF, phase retrieval and the CT reconstruction led to multiplication of the power spectrum by the square of the corresponding modulation transfer function (MTF). Therefore, by calculating noise power spectrum within the selected uniformly illuminated area of an image, we could determine the width of the MTF, and then calculate the width of the PSF assuming a certain general functional form of the PSF (Gaussian PSF is assumed in X-TRACT). The spatial resolution of the imaging system (including all the post-processing operations) was equated with the width of that PSF, referred back to the object plane (note that the x-ray source size had relatively minor contribution to the resolution in the used imaging configurations). After calculating both the SNR and the spatial resolution, we calculated their ratio, SNR/$\Delta r$, which, by definition, coincides with the product of the intrinsic quality characteristic $Q_s$ and the square root of the incident photon fluence (Gureyev *et al* 2014b). This product is reported as $Q'_S$ below. As the incident photon fluence was almost the same for all the images compared below, the multiplication of the intrinsic imaging quality by the square root of the fluence did not affect the comparison of the relative intrinsic quality of the images. The values of the indices obtained for iFBP and SIRT (1000 iterations) algorithms are presented in table 4. Additionally, the results for the spatial resolution and SNR are shown in figures 3 and 4. The solid lines correspond to linear fits to the data corresponding to images obtained with full phase retrieval, dashed lines correspond to images with half phase retrieval and dot-dashed lines correspond to images without the phase retrieval. Due to the large amount of the data, only results obtained inside the main lesion are presented.

Additionally, the degree of correlation between the results from the radiological assessment and calculated objective indices was analysed. Figure 5 reports the values of the quality index $Q_s$ compared with the radiological score, for the images reconstructed with the TIE-Hom algorithm. For the purpose of comparison with the radiological scores, the values of the $Q_s$ were divided by a fixed constant and shifted by another constant in order to account
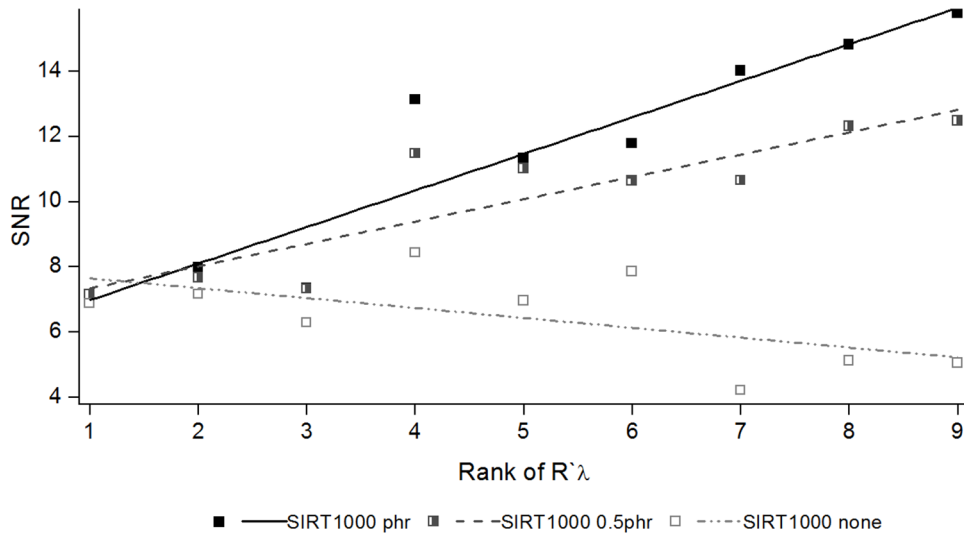
**Figure 4.** The values of SNR measured inside the lesion for images reconstructed with SIRT (1000 iterations) algorithm with none, half (0.5 phr) and full (phr) phase retrieval.
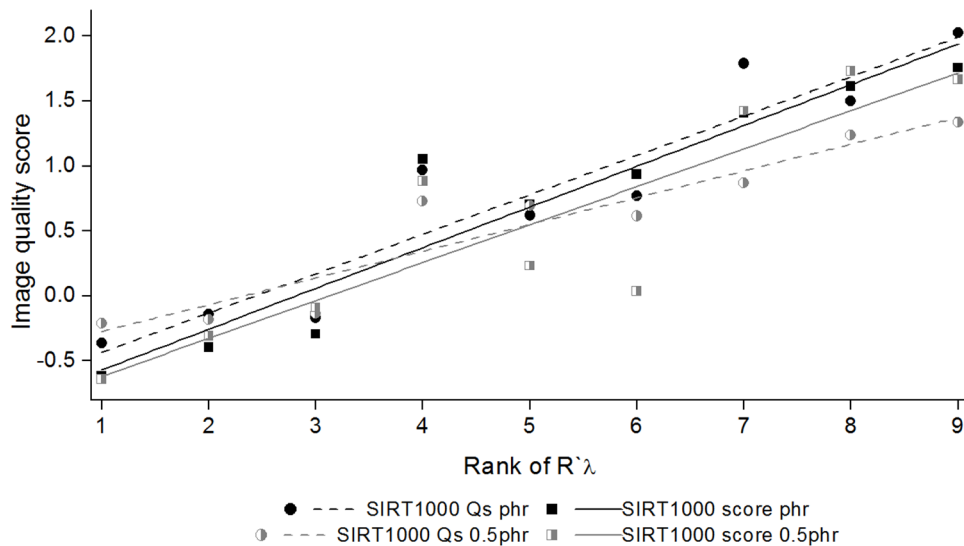


**Figure 5.** Correlation between the mean radiological score and the intrinsic quality characteristic ($Q_s$) for images obtained with SIRT (1000 iterations) algorithm with half (0.5 phr) and full (phr) phase retrieval.

for the difference in the scaling, between the original scale of $Q_s$ values (0 to $+\infty$) and the (*a priori* unrelated) scale of the average radiological scores ($-2$ to 2). Only results for the SIRT reconstructions (with 1000 iterations) are presented in figures 3–5 in order to avoid clutter. The trends for iFBP reconstructions were very similar. Results for other CT reconstruction algorithms will be presented in a further publication.
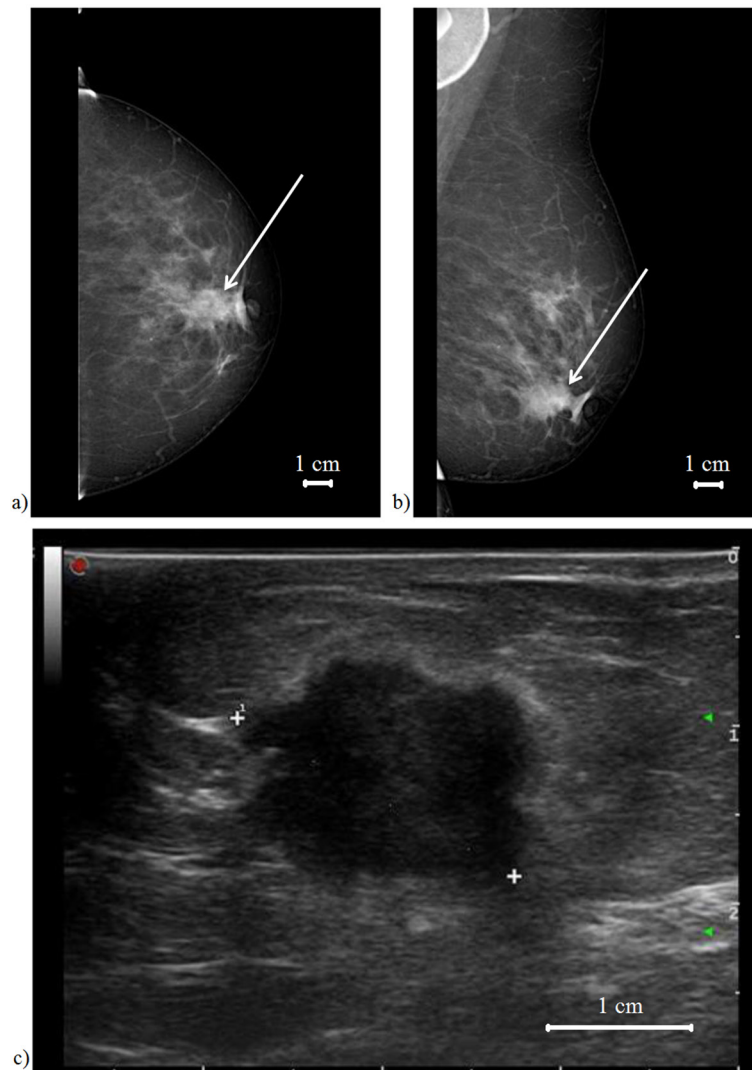
**Figure 6.** Mammographic and ultrasound images of the breast prior to mastectomy. (a) Digital mammography—the cranio-caudal view (CC) image (b) digital mammography—the mediolateral oblique view (MLO) image (c) result of ultrasonography examination.

*Comparison of the image features in the x-ray PB-CT and other types of images*

Mammography and ultrasound examination of the breast prior to the operation, which were performed as part of a standard diagnostic procedure, are shown in figure 6. The mammography examination showed an oval-shaped opacity with maximum diameter of 26 mm (figures 6(a) and (b)). The change visible in mammography was classified as R5 (according to breast imaging reporting and data system (BI-RADS) (Sickles *et al* 2013) indicating a high probability of breast cancer. The ultrasound examination (Hooley *et al* 2013) revealed a solid, inhomogeneous lesion, with maximum diameter of 23 mm (figure 6(c)). The result of this examination was classified as U5 (Mendelson *et al* 2013) which also means a high probability of breast cancer.
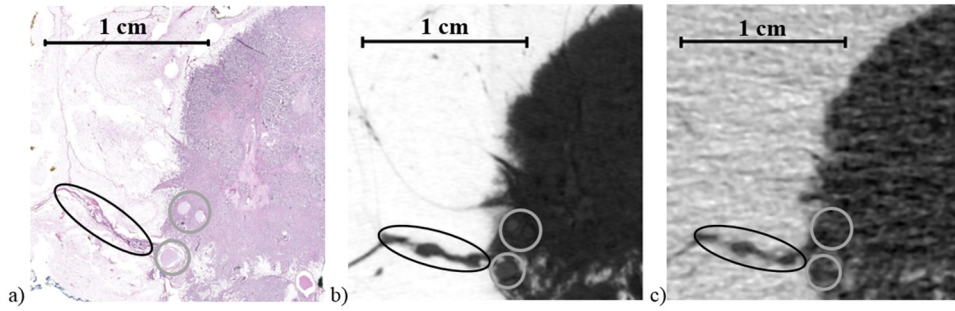
**Figure 7.** Images of the first part of the breast tissue sample. (a) Low-resolution histological section of the specimen. (b) High-quality phase contrast image obtained during the experiment with the dose of 1 Gy. (c) The best image according to radiological assessment with 4 mGy dose. Black ovals show fibrous stromal septa containing cribriform pattern ductal carcinoma *in situ*; grey ovals highlight benign cysts.
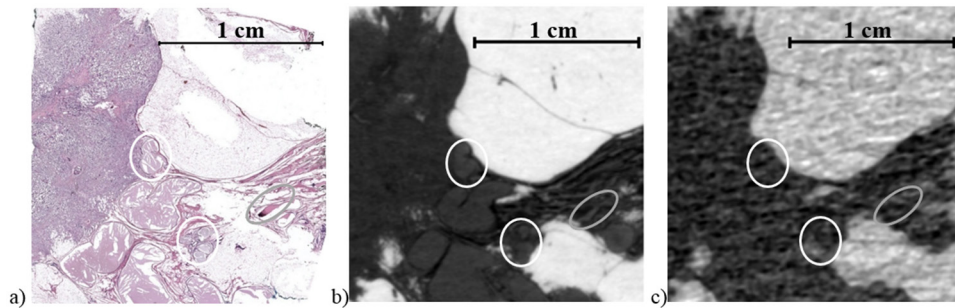


**Figure 8.** Images of the second part of the breast tissue sample. (a) Histological section of the specimen. (b) The best phase contrast image obtained during the experiment with 1 Gy dose. (c) The best image according to radiological assessment with 4 mGy dose. White ovals contain benign cysts; the grey oval highlights a blood vessel.

Histological examination of the sample is a gold standard for a reliable diagnosis of cancer and gives the final determination of the type of the cancer. For histological examination, the sample was cut into several parts suited for the histology preparation. For some of these histological images, the corresponding x-ray PB-CT images were identified. Comparison of three such images, which contained particularly interesting areas of the tumour and other lesions, are shown in figures 7–9. These images include histological sections as well as PB-CT images obtained with high and low radiation dose. The x-ray images are presented in the inverted grey-scale contrast in order to alleviate the comparison with the histological images. The high-dose images, shown in figures 7–9, were obtained at 9.31 m propagation distance and 38 keV energy using the Dalsa detector and were reconstructed using the FBP algorithm following the TIE-Hom phase retrieval with $\delta/\beta = 1083$. The low-dose images were collected with the Hamamatsu detector at 32 keV energy and 9.31 m distance and were reconstructed with iFBP algorithm following the TIE-Hom phase retrieval with $\delta/\beta = 870$. Both high- and low-dose images (figure 7) show clearly visible boundaries of the large lesion. The sharpness of these boundaries, more visible in figure 7(b), is one of the features important for tumour diagnosis. Internal structures of the lesion in histological section are qualitatively comparable
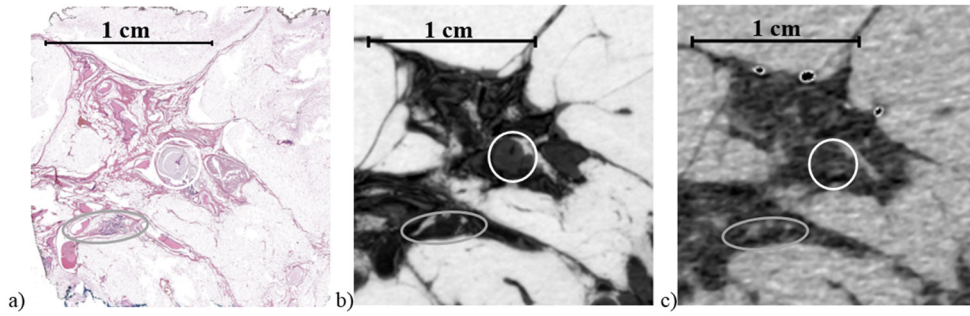
**Figure 9.** Images of the third part of the breast tissue sample. (a) Histological section of the specimen. (b) The best phase contrast image obtained during the experiment with 1 Gy dose. (c) The best image according to radiological assessment with 4 mGy dose. White ovals contain micropapillary pattern ductal carcinoma *in situ*, grey ovals contain areas of sclerosing adenosis.

to the grey scale variation in the high-dose image. Additionally, some of the spiculations are clearly visible. Furthermore, one of the spicules, marked by the oval in figure 7 was occupied by intraductal cribriform carcinoma. In the histological section, well-defined cystic lesions, which constitute fluid-filled sacs, are presented. In high-dose x-ray image, the cysts appear as darker (lighter, in the inverted contrast) areas with well-marked boundaries. The noise present in the low-dose image disrupts the image and makes the cysts indistinguishable.

The next area of the breast tissue sample shown in figure 8 contains the second part of the tumour, so previous comments about the margins of the lesion and the internal grey scale variation also apply. Apart from that, several large cysts with very clearly marked contours are visible in the high-dose image. Unfortunately, insufficient density difference in the low-dose image does not allow one to distinguish between the mass of the tumour and the cysts. Furthermore, blood vessels, clearly visible in the histological image, are not distinguishable in the low-dose x-ray image.

The last block of the specimen (figure 9) contains several spiculations clearly visible in both the high- and the low-dose x-ray images. Clear tissue differentiation is visible in both the histological image and the high-dose x-ray image. The most important features of this part of the sample are the suspicious areas of sclerosing adenosis. Unfortunately, these changes are not distiguishable in the x-ray images. Additionally, intraductal cribriform carcinoma area is visible in this part of the breast specimen.

## Discussion

Analysis of the data contained in table 4 and in figures 3–5 shows that, for images reconstructed with TIE-Hom algorithm, SNR, intrinsic image quality, $Q_S$, and the average radiological scores were all increasing according to the rank of the 'phase-contrast parameter', $R'\lambda$, while the spatial resolution remained relatively constant. In particular, the obtained radiological scores were consistently higher for the images collected with higher values of the phase-contrast parameter, in comparison with the reference image (which corresponded to the highest-quality reconstruction obtained without the phase contrast) at the same radiation dose. For larger sample-to-detector distances, the differences between the SNR value for the images with and without the application of the TIE-Hom phase retrieval algorithm became larger (up to 5 fold for $R_2 = 9.31$ m). The same trend was observed in the case of the intrinsic imaging quality, where the best results were achieved for the highest rank of $R'\lambda$. Comparison of the objective indices for images collected

at the same propagation distance, clearly showed the advantage of using the TIE-Hom algorithm compared to images reconstructed without phase retrieval, except for the lowest sample-to-detector distance where no obvious trend was found (the latter result was expected, as the degree of phase contrast in the projections collected at the shortest propagation distance was quite small). Moreover, at a fixed propagation distance, the best results were achieved in the present study for the lowest photon energy used, $E = 32$ keV. These results are in a good agreement with the previous theoretical and experimental results of x-ray phase contrast imaging (Keyriläinen *et al* 2011, Bravin *et al* 2013, Coan *et al* 2013, Gureyev *et al* 2014a, 2014b).

The validity of the representation by the obtained PB-CT images of some important morphological aspects of the breast tissue sample were confirmed by means of direct comparison with histological images (figures 7–9). Important features which define the lesions (sharpness of tumor boundaries or visibility of spiculations) could be clearly seen in both high- and low-dose images. Some fine details inside the lesion, such as cystic lesions or ducts were visible only in high-dose x-ray images. Unfortunately, because of the excessive dose, these high-dose images can be obtained only for excised samples, and not for live patients.

The present study was based on the analysis of a single tissue sample. However, we can state with confidence, based on other experiments and simulation studies using similar imaging techniques which involved many breast tissue samples with different types of tumors (Bravin *et al* 2013, Coan *et al* 2013, Gureyev *et al* 2014a, Nesterets *et al* 2015, Pacile *et al* 2015, Longo *et al* 2016), that the results reported here are relevant for generic PB-CT imaging of breast tissue. In particular, the results of earlier experiments, which included both formalin-fixed and fresh breast tissue (with blood), indicate that the formalin fixation process does not have significant effect on the quality of x-ray images of the tissues. In fact, according to our recent results, a slightly higher contrast can be achieved for unfixed tissue, compared to formalin-fixed tissue, in x-ray phase-contrast imaging (Hoshino *et al* 2014). Similar conclusions regarding the absence of significant effects of formalin fixation of tissues on x-ray phase-contrast image quality have been reported by other researchers (Willner *et al* 2015).

## Conclusion

Overall, the following main conclusions can be drawn from the present study:

(1) The PB-CT mammography method produces images with radiological quality that is consistently higher compared to the absorption-based images (i.e. the images similar to conventional mammography images, but collected here with a monochromatic beam instead of polychromatic x-rays used in conventional mammography systems) obtained at the same radiation dose, with the degree of improvement monotonically increasing with the 'phase-contrast parameter' $R'\lambda$.

(2) It has been also demonstrated, that the use of the TIE-Hom phase retrieval consistently improves both the radiological scores and the objective image parameters, such as SNR and $Q_s$, while only mildly affecting the spatial resolution.

(3) The (objective, no-reference) intrinsic image quality parameter, $Q_s$, appears to be in a good agreement with the average (subjective) radiological scores assigned to the images by experienced imaging specialists, particularly for the higher-quality images obtained with full phase retrieval.

According to these results, the PB-CT method, utilising large sample-to-detector propagation distances (9 m) and lower energy (32 keV) for image acquisition and TIE-Hom phase retrieval pre-processing in combination with iterative CT reconstructions, shows significant

promise for breast cancer imaging of live patients. The method is currently best suited for use at specialized synchrotron facilities, such as SYRMEP beamline at Elettra synchrotron, but can potentially be implemented in a clinical environment if sufficiently bright microfocus x-ray sources become available at a practical level. Substantial progress has been achieved in this area in recent years by introduction of novel types of compact microfocus sources using e.g. liquid metal jets, inverse Compton scattering and other physical mechanisms (Bech *et al* 2009, Larsson *et al* 2011), but further advances may be necessary before these sources attain the performance characteristics required for laboratory-based PB-CT imaging of live patients.

## Acknowledgments

## References

Alakhras M, Bourne R, Rickard M, Ng K H, Pietrzyk M and Brennan P C 2013 Digital tomosynthesis: a new future for breast imaging? *Clin. Radiol.* **68** e225–36

Bech M, Bunk O, David C, Ruth R, Rifkin J, Loewen R, Feidenhans'l R and Pfeiffer F 2009 Hard x-ray phase-contrast imaging with the compact light source based on inverse compton x-rays *J. Synchrotron Radiat.* **16** 43–7

Boin M and Haibel A 2006 Compensation of ring artefacts in synchrotron tomographic images *Opt. Express* **14** 12071–5

Bravin A, Coan P and Suortti P 2013 X-ray phase-contrast imaging: from pre-clinical applications towards clinics *Phys. Med. Biol.* **58** R1–35

Brun F, Accardo A, Kourousias G, Dreossi D and Pugliese R 2013 Effective implementation of ring artifacts removal filters for synchrotron radiation microtomographic images *8th Int. Symp. on Image and Signal Processing and Analysis* (IEEE) pp 672–6

Brun F, Pacilè S, Accardo A, Kourousias G, Dreossi D, Mancini L, Tromba G and Pugliese R 2015 Enhanced and flexible software tools for x-ray computed tomography at the Italian synchrotron radiation facility Elettra *Fundam. Inform.* **141** 233–43

Ciatto S *et al* 2013 Integration of 3D digital mammography with tomosynthesis for population breast-cancer screening (STORM): a prospective comparison study *Lancet Oncol.* **14** 583–9

Coan P, Bravin A and Tromba G 2013 Phase-contrast x-ray imaging of the breast: recent developments towards clinics *J. Phys. D: Appl. Phys.* **46** 494007

Dance D 1990 Monte-Carlo calculation of conversion factors for the estimation of mean glandular breast dose *Phys. Med. Biol.* **35** 1211

Diemoz P C, Bravin A and Coan P 2012 Theoretical comparison of three x-ray phase-contrast imaging techniques: propagation-based imaging, analyzer-based imaging and grating interferometry *Opt. Express* **20** 2789–805

Hoshino M, Uesugi K, Tsukube T and Yagi N, 2014 Quantitative and dynamic measurements of biological fresh samples with x-ray phase contrast tomography *J. Synchrotron Rad.* **21** 1347–57

Elmore J G, Armstrong K, Lehman C D and Fletcher S W 2005 Screening for breast cancer *J. Am. Med. Assoc.* **293** 1245–56

Ferlay J, Soerjomataram I, Dikshit R, Eser S, Mathers C, Rebelo M, Parkin D M, Forman D and Bray F 2015 Cancer incidence and mortality worldwide: sources, methods and major patterns in GLOBOCAN 2012 *Int. J. Cancer* **136** E359–86

Gazi P M, Aminololama-Shakeri S, Yang K and Boone J M 2016 Temporal subtraction contrast-enhanced dedicated breast CT *Phys. Med. Biol.* **61** 6322

Gureyev T, Mayo S, Nesterets Y I, Mohammadi S, Lockie D, Menk R, Arfelli F, Pavlov K, Kitchen M and Zanconati F 2014a Investigation of the imaging quality of synchrotron-based phase-contrast mammographic tomography *J. Phys. D: Appl. Phys.* **47** 365401

Gureyev T E, Nesterets Y I, de Hoog F, Schmalz G, Mayo S C, Mohammadi S and Tromba G 2014b Duality between noise and spatial resolution in linear systems *Opt. Express* **22** 9087–94

Gureyev T, Mohammadi S, Nesterets Y, Dullin C and Tromba G 2013 Accuracy and precision of reconstruction of complex refractive index in near-field single-distance propagation-based phase-contrast tomography *J. Appl. Phys.* **114** 144906

Gureyev T E, Nesterets Y, Ternovski D, Thompson D, Wilkins S W, Stevenson A W, Sakellariou A and Taylor J A 2011 Toolbox for advanced x-ray image processing *SPIE Optical Engineering + Applications* (International Society for Optics and Photonics) *Proc. SPIE* **8141** p 81410B

Hammerstein G R, Miller D W, White D R, Masterson M E, Woodard H Q and Laughlin J S 1979 Absorbed radiation dose in mammography *Radiology* **130** 485–91

Hooley R J, Scoutt L M and Philpotts L E 2013 Breast ultrasonography: state of the art *Radiology* **268** 642–59

Johns P C and Yaffe M J 1985 Theoretical optimization of dual-energy x-ray imaging with application to mammography *Med. Phys.* **12** 289–96

Keyrilainen J, Bravin A, Fernandez M, Tenhunen M, Virkkunen P and Suortti P 2010 Phase-contrast x-ray imaging of breast *Acta Radiol.* **51** 866–84

Keyriläinen J, Fernández M, Bravin A, Karjalainen-Lindsberg M-L, Leidenius M, von Smitten K, Tenhunen M, Kangasmäki A, Sipilä P and Nemoz C 2011 Comparison of *in vitro* breast cancer visibility in analyser-based computed tomography with histopathology, mammography, computed tomography and magnetic resonance imaging *J. Synchrotron Radiat.* **18** 689–96

Larsson D H, Takman P A C, Lundström U, Burvall A, and Hertz H M 2011 A 24 keV liquid-metal-jet source for biomedical applications *Rev. Sci. Instrum.* **82** 123701

Longo R *et al* 2016 Towards breast tomography with synchrotron radiation at Elettra: first images *Phys. Med. Biol.* **61** 1634–49

Mendelson E, Böhm-Vélez M, Berg W, Merritt C and Rubin E 2013 *ACR BI-RADS Atlas, Breast Imaging Reporting and Data System* (ACR BI-RADS® Ultrasound) pp 1–153

Michell M J, Iqbal A, Wasan R K, Evans D R, Peacock C, Lawinski C P, Douiri A, Wilson R and Whelehan P 2012 A comparison of the accuracy of film-screen mammography, full-field digital mammography, and digital breast tomosynthesis *Clin. Radiol.* **67** 976–81

Mittone A, Bravin A and Coan P 2014 Radiation dose in breast CT imaging with monochromatic x-rays: simulation study of the influence of energy, composition and thickness *Phys. Med. Biol.* **59** 2199–217

Myers G R, Thomas C D L, Paganin D M, Gureyev T E and Clement J G 2010 A general few-projection method for tomographic reconstruction of samples consisting of several distinct materials *Appl. Phys. Lett.* **96** 021105

National Electrical Manufacturers Association 2011 *Digital Imaging and Communications in Medicine (DICOM). Part 14 Grayscale Standard Display Function* (Arlington, VA: NEMA)

Nesterets Y I and Gureyev T E 2014 Noise propagation in x-ray phase-contrast imaging and computed tomography *J. Phys. D: Appl. Phys.* **47** 105402

Nesterets Y I *et al* 2015 A feasibility study of x-ray phase-contrast mammographic tomography at the imaging and medical beamline of the Australian synchrotron *J. Synchrotron Radiat.* **22** 1509–23

Olivo A *et al* 2013 Low-dose phase contrast mammography with conventional x-ray sources *Med. Phys.* **40** 090701

Pacile S *et al* 2015 Clinical application of low-dose phase contrast breast CT: methods for the optimization of the reconstruction workflow *Biomed. Opt. Express* **6** 3099–112

Paganin D, Mayo S C, Gureyev T E, Miller P R and Wilkins S W 2002 Simultaneous phase and amplitude extraction from a single defocused image of a homogeneous object *J. Microsc.* **206** 33–40

Pagot E *et al* 2005 Quantitative comparison between two phase contrast techniques: diffraction enhanced imaging and phase propagation imaging *Phys. Med. Biol.* **50** 709–24

Protection N C o R and Measurements 2004 (National Council on Radiation Protection and Measurements)

Sickles E, D'Orsi C, Bassett L, Appleton C, Berg W and Burnside E 2013 *ACR BI-RADS Atlas, Breast Imaging Reporting and Data System* (ACR BI-RADS® Mammography) pp 123–32

Siegel R L, Miller K D and Jemal A 2016 Cancer statistics, 2016 *CA: Cancer J. Clin.* **66** 7–30

Sztrokay A, Diemoz P C, Schlossbauer T, Brun E, Bamberg F, Mayr D, Reiser M F, Bravin A and Coan P 2012 High-resolution breast tomography at high energy: a feasibility study of phase contrast imaging on a whole breast *Phys. Med. Biol.* **57** 2931–42

Tromba G, Cova M A and Castelli E 2011 Phase-contrast mammography at the SYRMEP beamline of Elettra *Synchrotron Radiat. News* **24** 3–7

TS-Imaging Website 2016 www.ts-imaging.net/Services/Simple/ICUtilXdata.aspx (Accessed: 9 September 2016)

Van der Sluis A and van der Vorst H A 1990 SIRT-and CG-type methods for the iterative solution of sparse linear least-squares problems *Linear Algeb. Appl.* **130** 257–303

Willner M, Fior G, Marschner M, Birnbacher L, Schock J, Braun C, Fingerle A A, Noël P B, Rummeny E J, Pfeiffer F and Herzen J 2015 Phase-contrast hounsfield units of fixated and non-fixated soft-tissue samples *PLoS One* **10** e0137016

Zhao Y, Brun E, Coan P, Huang Z, Sztrokay A, Diemoz P C, Liebhardt S, Mittone A, Gasilov S, Miao J and Bravin A 2012 High-resolution, low-dose phase contrast x-ray tomography for 3D diagnosis of human breast cancers *Proc. Natl Acad. Sci. USA* **109** 18290–4